Matter

CellPress

Article

Curvature-Induced Modification of Mechano-Electrochemical Coupling and Nucleation Kinetics in a Cathode Material

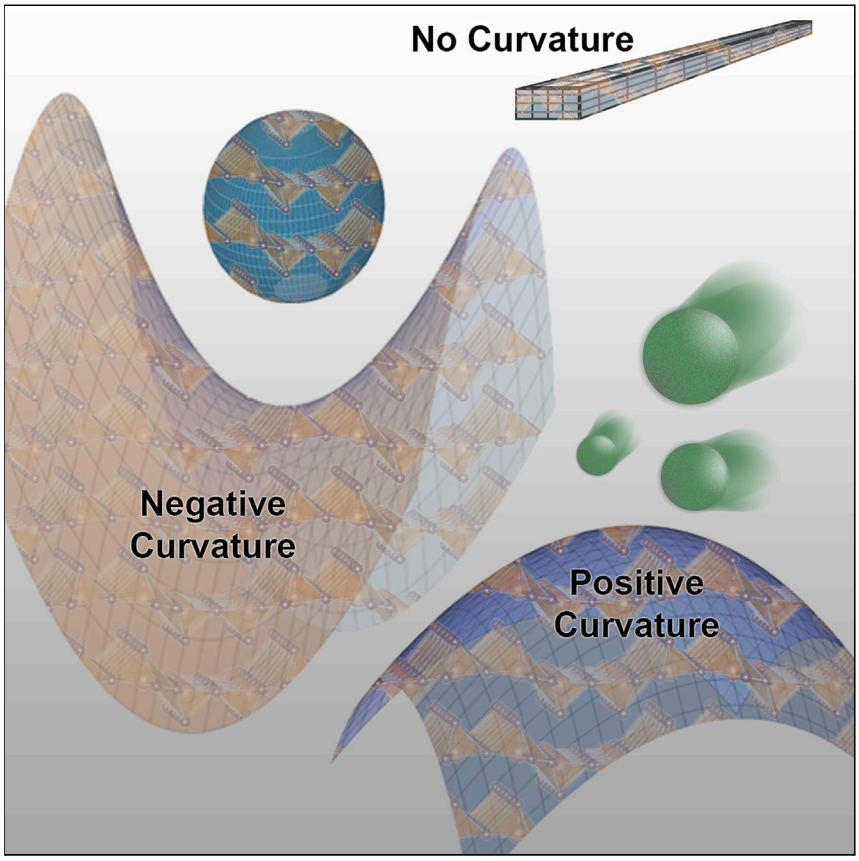

Justin L. Andrews, Peter Stein, David A. Santos, ..., James D. Batteas, Bai-Xiang Xu, Sarbajit Banerjee

xu@mfm.tu-darmstadt.de (B.-X.X.)
banerjee@chem.tamu.edu (S.B.)

HIGHLIGHTS

Preferential nucleation of lithiated domains at singular kinks within particles

Local curvature induces lithiation hot spots but engenders lattice coherency strain

Continuous curvature in 3D mesoscale architectures leads to single-phase lithiation

Continuous curvature mitigates coherency strain but enables fast diffusion kinetics

Lithium-ion batteries rely on the back-and-forth shuttling of lithium ions, which necessarily leads to expansion and contraction of electrode materials tasked with storing the ions. This expansion/contraction is taxing on battery materials, and the resulting stresses can nucleate microcracks, a key mechanism underpinning battery failure. In this work, we explore the role of particle curvature and defects across nanoscale and mesoscale dimensions as a means of leveraging relationships between chemistry and mechanics to mitigate intraparticle strain without sacrificing battery rate performance.

3 **Understanding**
Dependency and conditional studies on material behavior

Andrews et al., Matter 3, 1–20
November 4, 2020
https://doi.org/10.1016/j.matt.2020.08.030

Please cite this article in press as: Andrews et al., Curvature-Induced Modification of Mechano-Electrochemical Coupling and Nucleation Kinetics in a Cathode Material, Matter (2020), https://doi.org/10.1016/j.matt.2020.08.030

Matter

CellPress

Article

Curvature-Induced Modification of Mechano-Electrochemical Coupling and Nucleation Kinetics in a Cathode Material

Justin L. Andrews,[1,2,5] Peter Stein,[3,5] David A. Santos,[1,2,5] Cody J. Chalker,[1] Luis R. De Jesus,[1,2] Rachel D. Davidson,[1,2] Michelle A. Gross,[1] Matt Pharr,[4] James D. Batteas,[1,2] Bai-Xiang Xu,[3,*] and Sarbajit Banerjee[1,2,6,7,*]

SUMMARY

Intercalation-induced phase transformations in Li-ion battery electrode materials give rise to multi-phase coexistence regimes within individual particles, generating significant lattice coherency strain across dynamically evolving interfaces. We demonstrate here that the lattice coherency strain can be alleviated by leveraging the coupling of electrochemistry, mechanics, and particle geometry to achieve controllable nucleation and deterministic ion transport. Here, we contrast singular kinks and continuous curvature as a means of enabling homogeneous lithiation without developing large stresses within a model cathode material, V_2O_5. The singular kink confirms that local curvature facilitates lithiation but also exacerbates lithiation inhomogeneities and elastic misfit strain. In contrast, the incorporation of continuous curvature enables homogeneous single-phase lithiation, mitigating lattice coherency strain. The studies provide a direct view of the coupling of mechanics and electrochemistry within crystalline electrodes and suggest that mesoscale architectures can help resolve key failure mechanisms limiting the performance of energy-storage systems without sacrificing charge/discharge kinetics.

INTRODUCTION

Coupling between Electrochemistry and Mechanics in Electrode Materials

Lithium-ion (Li-ion) batteries rely on the coupled shuttling of Li ions and electrons between anode and cathode materials during battery charge and discharge.[1,2] The insertion and extraction of Li ions from an intercalation host drives the successive dilation and contraction of its crystal lattice. The intercalation-induced volumetric expansion and contraction of the electrode materials establishes a direct link between the mechanical properties of an intercalation host and its chemical reactivity. In addition to volume expansion, the insertion of Li ions in a cathode material during discharge of a battery further brings about reduction of the transition metal centers of the intercalation host. As a result of the population of non-bonding and anti-bonding states, the effective bond order is reduced and metal-ligand bond lengths are often observed to increase.[3,4] Local structural distortions derived from Li-ion insertion propagate across the crystal lattice in the form of highly directional lattice stresses. The accumulation of stresses can strongly affect the cycle life of cathode materials, resulting eventually in the fracture and delamination of active electrode materials.[5,6] The coupling of chemistry and mechanics has been widely studied for anodic conversion reactions

Progress and Potential

Failure mechanisms in intercalation batteries largely derive from mechanical stresses developed during cycling. Phase separation within individual electrode particles leads to substantial stresses arising from mismatched lattice dimensions at the boundaries separating differently lithiated domains, nucleating the formation of microcracks. Such phase separation is exacerbated at high rates. In this work, we have investigated the role of particle geometry on the homogeneity of lithiation and the resulting stress gradients. We show that by incorporating continuous geometric curvature, phase-pure lithiation of the cathode material can be achieved without sacrificing rate performance. This study illuminates the compounding effects of atomic-scale heterogeneities in originating mesoscale stresses and suggests that defining continuous curvature provides a means to achieve fast diffusion kinetics while alleviating the development of large stresses.

such as the alloying of silicon (where a dramatic ~300% volume expansion is observed)[7–10] and in cathode materials, where the intercalation-induced volume changes are comparatively modest (generally <8%) but nonetheless represent significant deformations for brittle ceramics.[9,11–17] While chemomechanical coupling has been widely studied, a practical means of designing electrode materials to harness these relationships so as to both improve diffusion kinetics and mitigate the consequences of volumetric expansion remains elusive. In this work, we use scanning transmission X-ray microscopy (STXM) and the spectroscopic signatures of differently lithiated phases to map the influence of curvature-induced lattice distortions on chemistry—mechanics coupling in a cathode material, orthorhombic V_2O_5—and further delineate the role of curvature in modifying nucleation kinetics in straight and kinked nanoribbons as well as continuously curved architectures.

The precise contours of intercalation-induced strain in cathode materials are governed by a number of intrinsic and extrinsic material properties including stresses developed from lattice mismatch with the substrate, inactive conductive additives, and intraparticle strain arising from phase segregation.[10,18–21] In the case of materials such as $LiFePO_4$ and V_2O_5 that exhibit miscibility gaps between Li-poor and Li-rich phases,[14,22–24] the coexistence of several distinct crystallographic phases with disparate unit cell volumes and incommensurate lattices within the same particles gives rise to significant lattice coherency strain.[22,23,25,26] Understanding the evolution of intraparticle strain from singular unit cell to mesoscale dimensions is critical to the design of mechanically resilient cathode architectures.

Attempts to address failure mechanisms stemming from the coupling of mechanics and electrochemistry[6,8,18,19,27,28] have focused on mitigating the consequences of lattice expansion through compositional modification (e.g., doping),[29,30] modulation of crystal structure and bonding through selection of polymorphs that avoid large displacive transformations,[11,31–34] the implementation of core-shell heterostructures to mitigate crack formation,[28,35] and the design of mesoscale architectures that are resilient to deformation under applied stresses.[17,36,37] Notably, the application of strain can accelerate or inhibit ion diffusion depending on the coupling of the strain fields with the crystal lattice. The relative displacement of atoms alters bond angles and bond lengths and thereby modifies both the electronic structure of strongly correlated systems and the coordination environments along ionic diffusion pathways.[4,32] In cathode materials, easing the coupled diffusion of Li ions and polarons in the form of self-trapped quasi-particles is critically important,[32,38–41] suggesting that strain represents a promising avenue by which electrode performance can be improved.[16,17,41] Yet only recently have the effects of lattice strain been systematically explored as a potential means of improving the functional performance of Li-ion batteries.[15,42] Pint and coworkers demonstrated that the application of a modest biaxial tensile strain in the *ab* plane of V_2O_5 (1.66%) can modulate the intercalation potential and improve the diffusion kinetics of Li ions by as much as 40 mV and 250%, respectively.[15] However, the promise of strain-induced performance improvements described in these works is limited practically by the need for epitaxial films for which strain is dissipated with increasing film thickness. Developing a means of incorporating elements of strain into powder electrodes, or alternatively for mitigating the evolution of intraparticle strain through the design of scalable mesoscale architectures, represents an important step toward leveraging mechanochemical coupling to improve battery performance.

[1]Department of Chemistry, Texas A&M University, College Station, TX 77843-3255, USA

[2]Department of Materials Science and Engineering, Texas A&M University, College Station, TX 77843-3255, USA

[3]Institute of Materials Science, Mechanics of Functional Materials, Technische Universität Darmstadt, Otto-Berndt-Strasse 3, Darmstadt 64287, Germany

[4]Department of Mechanical Engineering, Texas A&M University, College Station, TX 77840, USA

[5]These authors contributed equally

[6]Twitter: @SarbajitBanerj1

[7]Lead Contact

*Correspondence: xu@mfm.tu-darmstadt.de (B.-X.X.), banerjee@chem.tamu.edu (S.B.)

https://doi.org/10.1016/j.matt.2020.08.030

Please cite this article in press as: Andrews et al., Curvature-Induced Modification of Mechano-Electrochemical Coupling and Nucleation Kinetics in a Cathode Material, Matter (2020), https://doi.org/10.1016/j.matt.2020.08.030

Phase Inhomogeneities and Strain Evolution in the Orthorhombic V_2O_5 System

V_2O_5 represents a particularly interesting model cathode system as a result of its complex phase evolution upon Li-ion intercalation (Figures 1A and S1A). It is a quasi-layered material (Figure S1B) with multiple accessible redox states and is in principle capable of accommodating up to three Li ions per formula unit.[4] Despite its promise as a cathode material, orthorhombic V_2O_5 is plagued by sluggish electronic and ionic transport owing to the strong self-trapping of coupled (Li^+-[small polaron]) quasi-particles that contribute to the occurrence of multiple reversible (for $x < 1$ in $Li_xV_2O_5$) and irreversible (for $x > 1$ in $Li_xV_2O_5$) phase transitions (Figures S1B–S1E).[18,38,40] Indeed, the intercalation of Li ions into the layered structure of V_2O_5 induces several structural transformations, each accompanied by volume expansion, as summarized in Figure S1, with the δ-LiV_2O_5 phase approaching a volumetric expansion of 12.8% with respect to orthorhombic V_2O_5.[43] With increasing Li-ion insertion and localization of electron density, the apical oxygens of the VO_5 square pyramids are canted toward the inserted Li ions (black arrows in Figures S1C and S1D) and the V_2O_5 layers pucker, giving rise to a relatively small decrease in the crystallographic *a* parameter of the unit cell and a relatively large increase in the crystallographic *c* parameter of the unit cell (the crystallographic *b* parameter changes little across the entire phase space). This necessarily gives rise to anisotropic lattice distortions resulting in compressive and tensile strain, respectively, as the material alternately experiences contraction and expansion along different crystallographic directions. As has been noted in the case of Li_xFePO_4, boundaries between these distinct phases of $Li_xV_2O_5$, each having significantly different lattice parameters and thus molar volumes (Figure S1), exist within the same particle, thereby giving rise to substantial elastic misfit/coherency strain across the boundaries.[23,25,26]

STXM serves as a powerful nanoscale probe of electronic structure, enabling spatial domains with distinctive atomistic structure, chemical bonding, and disorder to be distinguished based on their individual spectroscopic signatures.[14,20,23,38,44,45] In this work, we map and contrast phase heterogeneities in V_2O_5 nanoribbons and mesostructured V_2O_5 three-dimensional (3D) architectures with increasing extents of curvature, comparing a straight V_2O_5 nanoribbon, a locally curved V_2O_5 nanoribbon, and a continuously curved interconnected V_2O_5 nanobowl architecture fashioned from colloidal crystal templating, shown schematically in Figure S2. The studies provide fundamental insight into the role of geometric curvature in altering ion-diffusion pathways and further illustrate a means of addressing the coupling of electrochemistry with mechanics to simultaneously accelerate kinetics of Li-ion diffusion while mitigating intercalation-induced stresses.

RESULTS AND DISCUSSION

STXM imaging has revealed significant interparticle[20] and intraparticle[14,38] phase inhomogeneities in V_2O_5 cathode materials. The observed inhomogeneities within individual particles derive in part from the barriers to coupled Li^+-(small-polaron) diffusion;[4,38,40] the trade-offs between surface-reaction-limited phase nucleation and propagation are further manifested as inhomogeneities across ensembles of particles ascribed to particle-by-particle lithiation (described as a "winner takes all" process) whereby sequential and not simultaneous lithiation is observed across collections of particles.[20,21] To map variations in electronic structure upon lithiation with high spectral and spatial resolution, we have used STXM to map chemical domains with increasing extents of curvature.[4,14,20,23,38,44] STXM images collected

Please cite this article in press as: Andrews et al., Curvature-Induced Modification of Mechano-Electrochemical Coupling and Nucleation Kinetics in a Cathode Material, Matter (2020), https://doi.org/10.1016/j.matt.2020.08.030

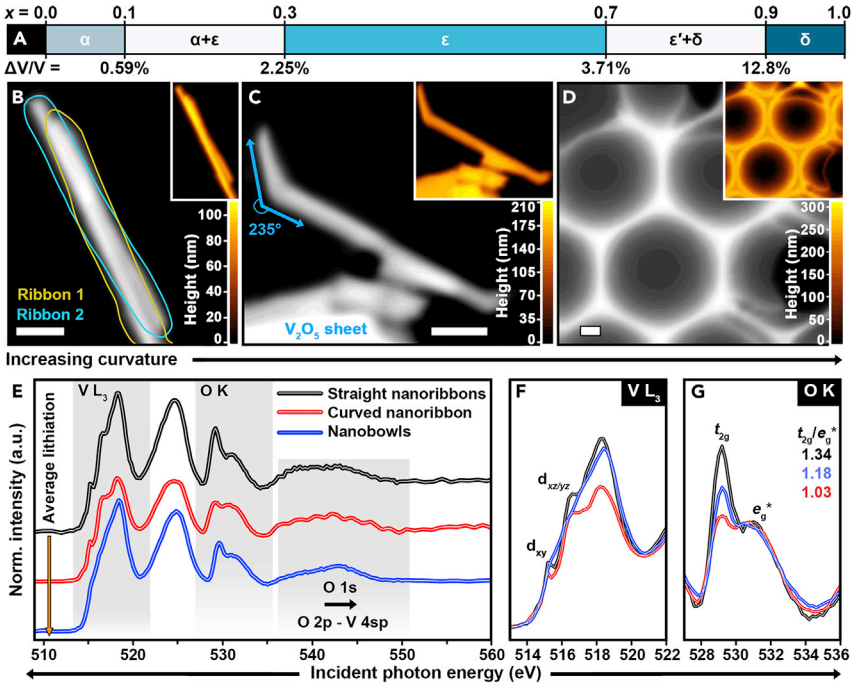

Figure 1. Working Out the "Kinks" in a V_2O_5 Cathode Material by Incorporating Curvature

(A–D) (A) Simplified phase diagram showing the evolution of unit cell volume expansion of α-V_2O_5 with increasing lithiation. A more detailed phase diagram compiled from an extensive review of the literature is provided in Figure S1A. STXM optical-density images collected for (B) two closely overlapped straight V_2O_5 nanoribbons; (C) a locally curved "kinked" V_2O_5 nanoribbon; and (D) a continuously curved V_2O_5 nanobowl architecture prepared by colloidal crystal templating. A schematic clearly delineating 3D interconnected nanobowls is provided in Figure S2. The light-blue and gold contours in (A) outline the boundaries of two overlapping nanoribbons. In (B), a V_2O_5 sheet situated near the curved/strained nanoribbon is also labeled. Thickness maps generated by normalization of the STXM image to an elemental profile are shown inset to (B), (C), and (D). High-resolution thickness maps are provided in Figure S3, and a direct comparison of thickness profiles for the various geometries is provided in Figure S3D. Scale bars, 500 nm.

(E) Integrated spectra obtained by averaging the spectra embedded at all pixels in the images in (B) to (D). The integrated spectra are arranged in order of increasing overall or "average" extent of lithiation (top to bottom).

(F and G) Regions of the (F) V L_3-edge and (G) O K-edge spectra are shown in greater detail.

for straight/unstrained nanoribbons, a locally curved nanoribbon, and a continuously curved V_2O_5 architecture are shown in Figures 1B–1D.

V_2O_5 nanoribbons were synthesized according to a previously reported method as described in detail in Experimental Procedures,[46] and were determined to be phase pure by powder X-ray diffraction (Figure S4A). The nanoribbons exhibit rectangular cross-sections with widths on the order of tens of nanometers and lengths on the order of several micrometers (Figures S4B–S4I depict cross-sectional views of the nanoribbons illustrating their flat surfaces). The rectangular crystal habit is consistent with the orthorhombic crystal structure of α-V_2O_5. STXM further enables the visualization of sample thicknesses by normalization of data collected in transmission mode, as detailed in Experimental Procedures. Height maps for the straight nanoribbon, locally curved nanoribbon, and the continuously curved V_2O_5 architectures prepared by colloidal crystal templating are shown inset to the STXM images in Figures 1B—1D.

Figure S5 delineates the process for placing these materials onto silicon nitride grids where they are chemically lithiated using *n*-butyllithium. Each of the materials has been lithiated under the same conditions to facilitate direct comparison of observed lithiated domains (i.e., the materials were subjected to the same concentration of *n*-butyllithium and the same reaction time, as described in more detail in Supplemental Experimental Procedures). The relatively short lithiation time used here ensures that the nanoribbons are not lithiated to completion and enables the viewing of a non-equilibrium "snapshot" of the early stages of lithiation where compositional inhomogeneity is significant. Statistical image analysis tools, including principal component analysis (PCA), pixel-clustering analysis, and singular value decomposition (SVD), are used to obtain rich quantitative chemical maps of lithiated domains that further enable mapping of stress across individual particles, as shown in Figure S6.

Integrated spectra obtained by averaging across all the pixels in each image are shown in Figure 1E. Three regions of the X-ray absorption spectroscopy (XAS) spectra are highlighted, corresponding to excitations of core electrons: the V L_3-edge absorption (513–522 eV) arises from transitions from singlet V $2p^6 3d^0$ to V $2p^5 3d^1$ states that are further split by crystal field and multiplet effects; the O K-edge X-ray absorption features (527–536 eV) arise from transitions from O 1s core levels to hybrid V 3d—O 2p states, which are further split by quasi-octahedral (i.e., VO_{5+1}) crystal field splitting into t_{2g} and e_g* manifolds; and a broad feature that arises from transitions from occupied O 1s states to unoccupied hybridized O 2p–V 4sp states (535–550 eV).[47] The line shapes at the V L_2-edge (521–529 eV) are dominated by a Coster-Kronig Auger decay process from an occupied $2p_{1/2}$ state into the $2p_{3/2}$ hole and are therefore difficult to interpret in terms of electronic structure.[38,47] The relative intensities, line shapes, peak positions, and splitting observed at the V L_3-edge and O K-edge t_{2g}/e_g* manifold provide a rich view of the evolution of lithiated phases in V_2O_5 materials.[4,14,31,38,45] As such, expanded views of these regions are provided in Figures 1F and 1G and throughout this article. The V L_3-edge comprises two prominent features corresponding to transitions from occupied V 2p core levels to unoccupied states with V $3d_{xy}$ (split-off conduction band)[38,47] and V $3d_{xz/yz}$ character at the bottom of the conduction band of V_2O_5 (centered at 515.2 and 516.4 eV, respectively). The spectral intensity of these absorption features is directly correlated with the availability of empty states; the features are most intense prior to lithiation as a result of the nominally d^0 character.[34] Upon Li-ion intercalation, electrons have been shown to localize in the narrow V $3d_{xy}$ split-off conduction band, which is separated by a small gap from the bottom of the conduction band.[4,38,40] Indeed, such electron localization within narrow $3d_{xy}$ states is a characteristic signature of small polaron formation. Consequently, with increasing extent of lithiation, previously unoccupied V $3d_{xy}$ states are filled by electrons, and the spectral features derived from these empty states "darken" and diminish in intensity owing to Pauli blocking.[38] The same trend is observed for the $d_{xz/yz}$ feature, highlighted in Figure 1F, which similarly "darkens" at still higher levels of lithiation. The sensitivity of the fine structure at the V L_3-edge provides a means to evaluate the pixel-wise extent of lithiation.

The O K-edge region is similarly informative in assessing the extent of lithiation and the evolution of electronic structure, but for entirely different reasons.[38] The O K-edge spectra are not convoluted by multiplet effects and exhibit two sets of transitions from O 1s to hybrid V 3d–O 2p states, closely approximating the t_{2g} and e_g* character expected from the crystal field splitting for a quasi-octahedral VO_{5+1} structure. Based on time-dependent density functional theory (TD-DFT) calculations,

Please cite this article in press as: Andrews et al., Curvature-Induced Modification of Mechano-Electrochemical Coupling and Nucleation Kinetics in a Cathode Material, Matter (2020), https://doi.org/10.1016/j.matt.2020.08.030

the t_{2g} absorption features are attributed primarily to transitions from O 1s core states of the V=O oxygens in VO_5 square pyramids to O $2p_x/2p_y$ states hybridized with V $3d_{xz}$ and $3d_{yz}$ states (with a much more modest contribution derived from transitions from O 1s core levels of bridging oxygen atoms to O $2p_y$ states mixed with V $3d_{xy}$ states). The relative ratio of the t_{2g}-to-e_g* features serves as a key diagnostic of the extent of Li intercalation. The diminution of the t_{2g} feature intensity with increasing lithiation results not from Pauli blocking as in the case of the fine structure at the V L_3-edge, but from the strong distortion and lengthening of the V=O vanadyl bonds illustrated in Figures S1B and S1C along with incipient electron correlation as the V $3d_{xy}$ band is partially filled. The emergence of electron correlation results in a lifting of spin degeneracy and the spin-splitting of the V 3d states, which brings about a sharp decrease in the intensity of the primary t_{2g} absorption band. The distortion of the vanadyl moieties also shifts the V $3d_{xz}$ states to higher energies, resulting in the spectral weight diminishing in the t_{2g} manifold and being shifted to higher energies. As such, the ratio of the intensities of the t_{2g}-to-e_g* manifolds is observed to decrease with increasing extent of lithiation. These ratios are provided throughout this work to facilitate comparison of spectra. The final highlighted region corresponds to transitions from O 1s to hybridized O 2p–V 4sp states.[20] STXM data and spatially resolved spectra will be interpreted on the basis of these assignments and on the basis of previously reported V L-edge, O K-edge spectra collected for stoichiometrically lithiated $Li_xV_2O_5$ materials that allow for assignment of relative spectral intensities at both the V L-edge and the O K-edge to the extent of lithiation x in $Li_xV_2O_5$.[38]

Notably, despite following the same chemical lithiation procedures and conditions (i.e., reagent concentration, lithiation time), substantial differences are observed in the integrated spectrum acquired for each sample, plotted in Figure 1E. The spectra compared in Figures 1E–1G are "average" spectra in the sense that they are obtained by integrating the spectra obtained from every pixel present in the STXM image and, thus, each $Li_xV_2O_5$ phase present within the imaged material. As such, they are composite spectra comprising spectra from each phase present in the material, weighted by the number of imaging elements containing that phase. This is distinct from the spectra shown in Figures 2, 3, and 4 (vide infra), which are obtained by principal component clustering analysis of the spectra and more accurately reveal spatial distribution of differently lithiated phases within individual particles. The spectra are arranged in order of increasing extent of lithiation from top to bottom as evidenced by decreasing intensity of the V $3d_{xy}$ and $3d_{xy/yz}$ features. Although both the V L_3-edge and O K-edge regions (as shown in Figures 1F and 1G, respectively) are used to assign extent of lithiation throughout this paper, since the integrated spectra shown in Figure 1 are composite spectra integrated across the entire image, the intensity of the V L_3-edge can most reliably be used to interpret the average extent of lithiation, since the darkening of V L_3-pre-edge features can be used as a direct means of evaluating the formal vanadium oxidation state or state of charge. A methodology for quantitative assignment of the extent lithiation at each pixel (instead of average lithiation of the imaged sample) with reference to standards is delineated below.

Critically, the increase in the extent of lithiation does not track with decreasing diffusion path length (Figure S3D), but rather follows the opposite trend since the much thicker 3D nanobowl architecture is most lithiated. Figure S3D shows that the width of the straight nanoribbon is smaller than the kinked nanoribbon. Both are far smaller than the width of the continuously curved 3D architecture, even nearing its thinnest point (i.e., the ridge between two bowls). Contrary to what is expected from simple

Please cite this article in press as: Andrews et al., Curvature-Induced Modification of Mechano-Electrochemical Coupling and Nucleation Kinetics in a Cathode Material, Matter (2020), https://doi.org/10.1016/j.matt.2020.08.030

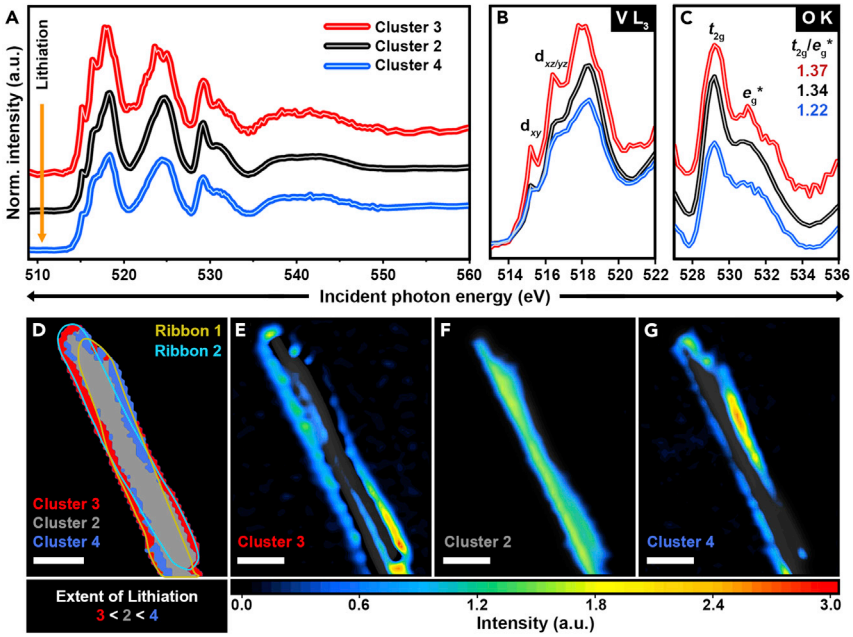

Figure 2. Core-Shell Inhomogeneity in Straight V_2O_5 Nanoribbons

(A) Spectra derived from clustering of pixels scored using PCA of the STXM image of an unconstrained pair of straight nanoribbons upon lithiation (Figure S6 outlines the data-processing workflow). The pre- and post-edge normalized spectra are ordered according to increasing lithiation (top to bottom).

(B and C) Evolution of (B) V L_3-edge features (513–522 eV) and (C) O K-pre-edge features (527–536 eV).

(D) Spatial grouping of the spectra in (A) according to PCA, where the apparent extent of lithiation increases going from red to gray to blue.

(E–G) Intensity maps showing the weighted contribution of the spectra in (A) to each pixel in the STXM image. The Cluster 3 map (E) corresponds to the red spectrum, the Cluster 2 map (F) corresponds to the black spectrum, and the Cluster 4 map (G) corresponds to the blue spectrum. The colored legend quantifies the relative weighting of the cluster spectra at each pixel. The maps are in order of increasing lithiation. Figures S7 and S8 depict the ROI and PCA analysis used to identify distinctive lithiated domains and develop the phase maps.

Scale bars, 500 nm.

consideration of diffusion path lengths alone, the thickest material is the most highly lithiated for the same lithiation conditions. The straight/unstrained nanoribbons (Figure 1B) exhibit a relatively low extent of lithiation, whereas the locally curved nanoribbon (Figure 1C) exhibits an average extent of lithiation intermediate between the two (albeit with substantially greater inhomogeneity, as will be discussed below). The continuously curved V_2O_5 architecture exhibits a markedly greater extent of lithiation compared with the nanoribbons, as evidenced by the complete disappearance of all fine structure at the V L_3-edge, characteristic of the formation of a highly lithiated ε-$Li_xV_2O_5$ phase ($x = 0.6$).[4,14,20,38,47] Given the identical lithiation conditions, it follows that the observed rate of lithiation of the V_2O_5 materials in Figures 1B–1D instead correlates to increasing curvature. The observed relationship between increasing lithiation rates at higher curvatures parallels the effects of applied strain.[15,42] Mapping of mesoscale domain formation through region of interest (ROI) analysis, PCA, and SVD provide meaningful insight into the spatial distribution of lithiated phases between and within individual particles. The STXM images collected for the three particle morphologies shown in Figures 1B–1D are evaluated using these techniques in greater detail below. The role of geometric curvature in

Please cite this article in press as: Andrews et al., Curvature-Induced Modification of Mechano-Electrochemical Coupling and Nucleation Kinetics in a Cathode Material, Matter (2020), https://doi.org/10.1016/j.matt.2020.08.030

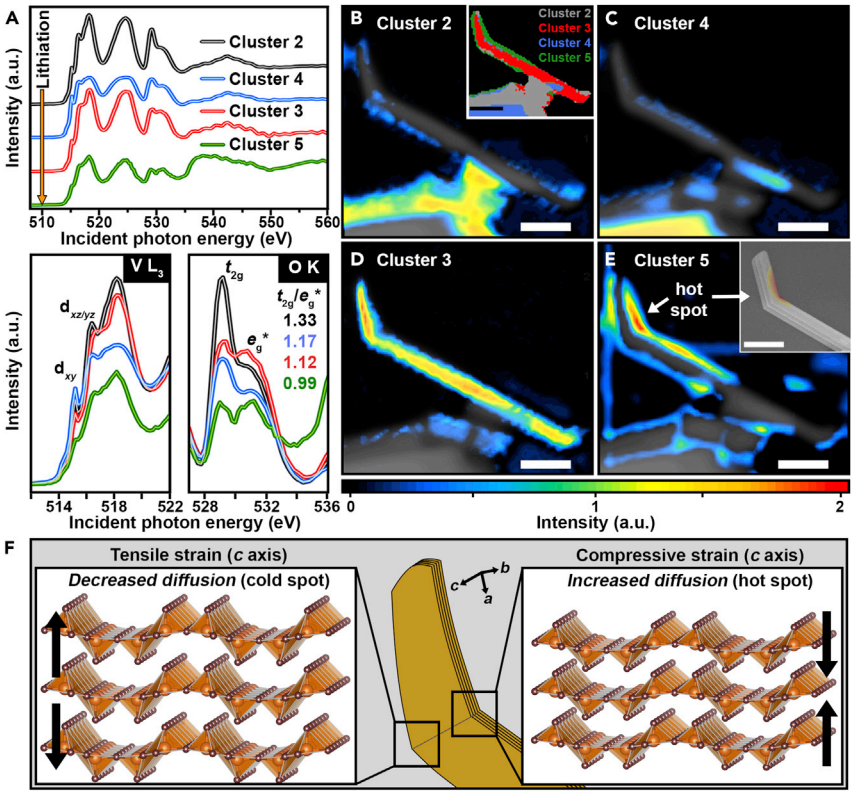

Figure 3. Curvature-Induced "Hot-Spot" Formation in a Bent V_2O_5 Nanoribbon

(A) Spectra obtained by PCA clustering of the pixels for the locally curved nanoribbon shown in Figure 1C. The pre- and post-edge normalized spectra are offset in order of increasing lithiation (top to bottom). The lower panels highlight the V L_3-edge features (513–522 eV) and the O K-pre-edge features (527–536 eV), respectively.

(B–E) Intensity maps generated using the PCA-clustering-derived spectra in (A) as input. The maps are in order of increasing lithiation. The PCA-clustering image (also shown in Figure S15) is shown inset to (B). A SEM image of the ~45° kink in the nanoribbon is shown inset to (E), where the hot-spot location formation is overlaid in false color. Scale bars, 500 nm.

(F) Schematic detailing the mechanistic origins of "hot spot" and "cold spot" formation in the locally curved V_2O_5 nanoribbon.

enhancing lithiation is discussed with regard to anisotropic lattice expansion of the V_2O_5 material and its concomitant directional change of Li-ion diffusivity.

Surface-Limited Inhomogeneous Lithiation in a V_2O_5 Nanoribbon

Figure 1B shows the optical density STXM image for two overlapped straight nanoribbons representing the no-curvature condition. ROI analysis of these unstrained nanoribbons, provided in Figure S7, reveals compositional inhomogeneities, particularly when contrasting the spectra obtained by integrating near the end of the first nanoribbon (labeled as ROI-3 and ROI-5) and the spectra obtained for the interior of the nanoribbon (labeled as ROI-1). To develop a more detailed perspective of the local phase distribution, we performed PCA (Figure S8)[14,38,48] and coupled this with pixel-clustering analysis (PCA-clustering analysis) (Figure 1D) to enable the comparison of the spatial distribution of spectrally similar XAS spectra (e.g., in Figure 1B).[48] These spectra are distinct from the spectra shown in Figure 1 (which are integrated spectra) in that they delineate distinct regions of the material that have spectral features which are clustered on the basis of their similarity. Interpretation

Please cite this article in press as: Andrews et al., Curvature-Induced Modification of Mechano-Electrochemical Coupling and Nucleation Kinetics in a Cathode Material, Matter (2020), https://doi.org/10.1016/j.matt.2020.08.030

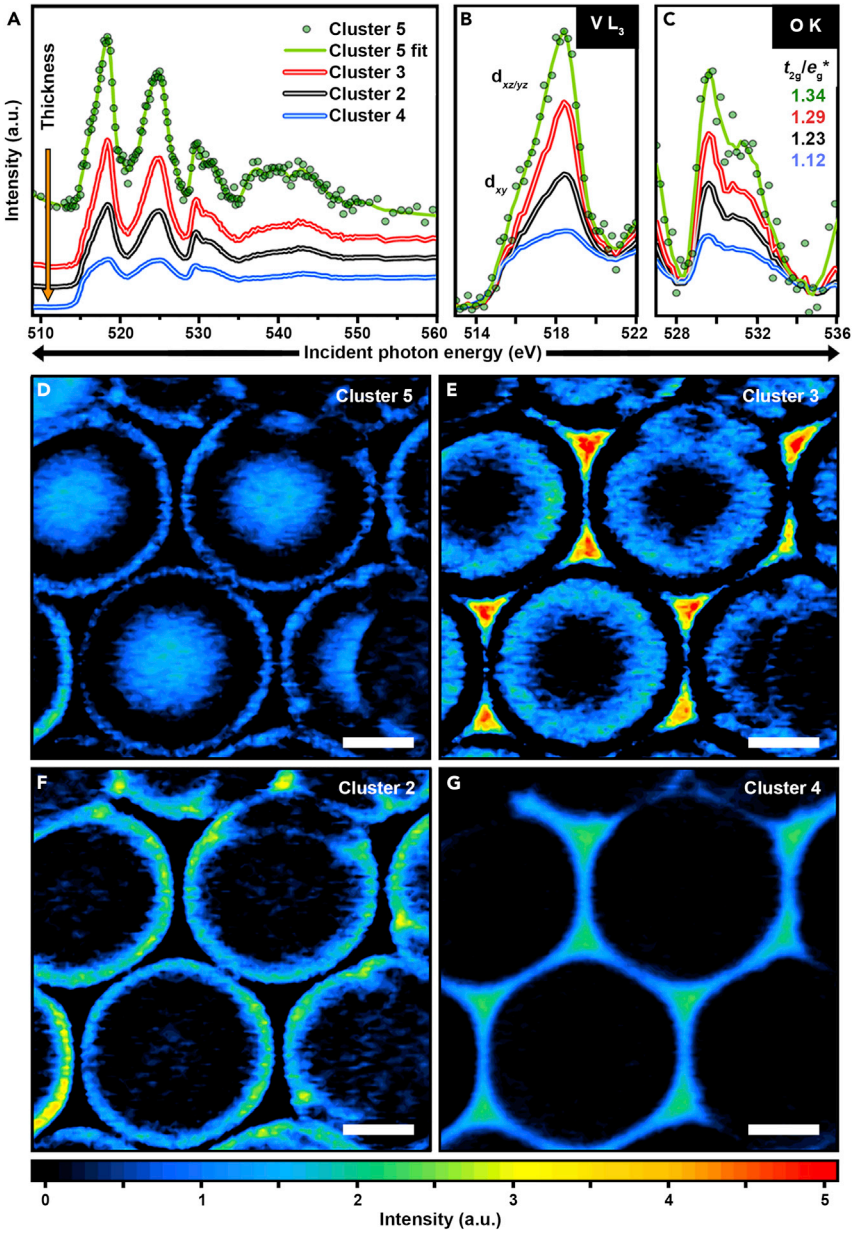

Figure 4. Rapid Lithiation and Improved Homogeneity in Continuously Curved V_2O_5 Interconnected Nanobowl Architectures

(A) Spectra obtained by PCA clustering of the continuously curved V_2O_5 architecture STXM image shown in Figure 1D. The pre- and post-edge normalized spectra are offset in order of increasing thickness (top to bottom).

(B and C) Expanded regions of (B) V L_3-edge features and (C) O K-pre-edge features.

(D–G) Intensity maps obtained using the spectra in (A) as input. The map panels are arranged in order of increasing thickness (left to right, top to bottom). Figures S17–S19 show the ROI and PCA analysis used to identify distinctive lithiated domains and develop the phase maps. The spectrum (Cluster 4) corresponding to the thickest parts of the sample shows evidence of detector nonlinearity as a result of thickness effects. Examples of additional nanobowl architectures are provided in Figures S20 and S21. Scale bars, 1 μm.

Please cite this article in press as: Andrews et al., Curvature-Induced Modification of Mechano-Electrochemical Coupling and Nucleation Kinetics in a Cathode Material, Matter (2020), https://doi.org/10.1016/j.matt.2020.08.030

of the clustered spectra in Figures 2A–2C reveals that the regions corresponding to cluster 4 are most lithiated, whereas the regions corresponding to cluster 3 are least lithiated. The spatial arrangement of the clusters indicates that the smaller nanoribbon (ribbon 1, ~270 nm in width) is more highly lithiated as indicated by localization of the blue component around the visible edges of the ribbon. In contrast, ribbon 2 (~330 nm in width), which is viewed parallel to the basal planes (down the layer stacking direction, as shown in Figure S9), shows core-shell lithiation with the edges being sparsely lithiated and the interior showing a relatively higher extent of lithiation. The observation of core-shell behavior derives from the specific orientation of the nanoribbons on the substrate as described in greater detail in Figure S9, and is further consistent with surface-limited lithiation along the direction between the V_2O_5 layers and limited Li-ion insertion transverse to the layers.[14,20] The PCA-clustered spectra obtained for this sample (Figures 2A–2C) were used as input spectra for SVD analysis, as shown in Figures 2E and 2F, which further elucidate the contributions of the input spectra to the spectrum at each pixel in real space. Both nanoribbons exhibit core-shell behavior but ribbon 1 is overall more lithiated (ε-$Li_{0.3}V_2O_5$ and α-$Li_{0.1}V_2O_5$), whereas ribbon 2 is less lithiated (α-$Li_{0.1}V_2O_5$ and α-V_2O_5). As shown in Figure S1, these compositions correspond to nearest neighbors in the phase diagram. The origins of the different extents of lithiation for the nanoribbons derive in part from geometric irregularities (which drive preferential lithiation fronts)[49] compounded by particle-by-particle lithiation, since the wires are in close contact.[20,21,50] In a reaction-limited regime as is typical of lithiation in phase-separating electrodes,[51,52] geometrical features such as sharper edges for the thinner nanowire can drive heterogeneities, altering the local ionic flux that mediates the preferential initiation and propagation of reaction fronts and compounded further by hot spots arising from kinetic, ohmic, and entropic processes.[51,53] Critically, multi-phase core-shell behavior within individual particles induces a significant amount of elastic misfit strain at the interface between $Li_xV_2O_5$ phases as a result of lattice incommensurability and the differential in the volumes of the two dilated phases with varying extents of lithiation (Figures 1A and S1).[14,15,43,54] Figure S10 exhibits additional examples of the core-shell motif observed for straight nanoribbons upon lithiation.[14,38] Core-shell behavior has further been evidenced across ensembles of nanoribbons by using Raman spectroscopy to probe surface lithiation and powder X-ray diffraction (XRD) to probe nanoribbon interiors.[46] For thin nanoribbons, wherein the scaling factor of the elastic misfit penalty is low, charge-stripping behavior has been evidenced, characterized by the appearance of periodic nanoscopic domains as a result of coherency strain.[26] We have next mapped the effects of curvature on the spatial organization of lithiation patterns in both individual nanoribbons and continuously curved architectures, with a view toward correlating lithiation patterns with accumulated stresses.

Curvature-Assisted Lithiation Induces "Hot Spot" in a Bent V_2O_5 Nanoribbon

Hydrothermal synthesis yields a notable fraction of nanoribbons with bent defects (Figures 1C, S11, and S12) that have the potential to induce anisotropic stress fields and thereby modify the kinetics and, consequently, the spatial distribution of lithiation. Several such kinks have been shown to profoundly modify the spatial distribution of lithiation within individual particles,[20] but a quantitative mapping with high spatial resolution has not thus far been performed. Several such nanoribbons incorporate defects that induce one or more (Figure S11) approximately 45° kinks along the V_2O_5 basal plane. Transmission electron microscopy (TEM) images shown in Figure S12 clearly evidence stacking faults that induce a change in growth direction and the introduction of accompanying local curvature. Figure S13 shows a scanning electron microscopy (SEM) image (also included as an inset to Figure 3E) of the curved

Please cite this article in press as: Andrews et al., Curvature-Induced Modification of Mechano-Electrochemical Coupling and Nucleation Kinetics in a Cathode Material, Matter (2020), https://doi.org/10.1016/j.matt.2020.08.030

nanoribbon corresponding to the STXM image shown in Figure 1C, which has been lithiated "on-substrate" using conditions exactly paralleling the straight nanoribbons in Figure 2 as per the workflow described in Figure S5. The nanoribbon exhibits a singular ~45° kink near one terminus, likely derived from a stacking fault. As discussed above and shown in Figure 1, the curved nanoribbon exhibits an overall greater extent of lithiation as compared with the unstrained nanoribbon (Figure 2); however, the integrated spectrum shown in Figure 1E does not accurately represent the vastly different lithiation extents across the curved nanoribbon. The bent nanoribbon was lithiated and analyzed by STXM (Figure 3). ROI analysis of hyperspectral STXM data shown in Figure S14 reveals significant local inhomogeneities within the V_2O_5 nanoribbon, as evidenced by substantial changes in fine structure at the V L_3-edge and large variations of the t_{2g}/e_g* ratios at the O K-edge (Figure 3A).

PCA-cluster analysis performed for the curved nanoribbon is shown in Figure S15 and highlights the spatial distribution of distinctive lithiated domains, as also shown in the inset to Figure 3B. PCA-clustering analysis suggests that the nanoribbon is significantly more lithiated at or around the inside of the kink (i.e., cluster 5, green, corresponding to an area under residual compressive stress) as compared with the rest of the nanoribbon and adjacent sheet (i.e., regions corresponding to clusters 3 and 4). There further appears to be a small region of relatively unlithiated V_2O_5 on the outside of the kink of the nanoribbon (i.e., cluster 2, corresponding to an area under tensile strain).

Figures 3B–3E map the results of SVD analysis performed using the PCA-clustered spectra shown in Figure 3A as input. The nanoribbons, which grow with kink defects, likely have residual strain around the defects; the inner edge of the defect, which is likely to be under compressive strain, is found to be the most lithiated region of the nanoribbon as shown in Figure 3E, revealing the formation of a "hot spot." In contrast, the outer edge of the kink in the nanoribbon (which is likely under residual tensile strain) shows a well-defined band corresponding to low levels of lithiation (cluster 2), representing a "cold spot." The adjacent, much thicker, sheet is also sparsely lithiated. In other words, clear "hot" and "cold" spots can be resolved at concave and convex regions of the curved nanoribbon, respectively. The formation of a hot spot in the vicinity of a region of compressive strain is somewhat counterintuitive, since most materials have been shown to exhibit decreased ionic diffusion when subject to compressive strain.[16,17,41] However, the sign (i.e., positive or negative) of the coupling between strain and Li-ion diffusion is dependent on the crystal structure and crystal orientation and is determined by the coupling of these attributes with the directionality of the strain vector. Indeed, compressive strain along the *c* axis in V_2O_5 (corresponding to the interlayer spacing) has been shown to dramatically improve Li-ion diffusivity and, conversely, tensile strain along the *c* axis has been shown to decrease Li-ion diffusivity.[15] TEM images of a kink defect in Figure S12 suggest that the kink in the nanoribbon is along the *ab* plane, corresponding to compression of the *c* direction along the interior of the kink. This is shown schematically in Figure 3F.[4,31,32] It is furthermore likely that the kink, which alters the strain field in its vicinity, further acts as a nucleation site for the kinetically limited lithiation phenomenon. The generation of a compositional hot spot in the vicinity of the kink, which is spatially confined, likely contributes to a lithiation "feedback loop." Increased lithiation of the concave side of the nanoribbon as a result of residual compressive strain causes the material to expand into a spatially constrained area, further generating stress concentrators in response to the reaction front.[55] The increased compressive stress further increases the rate of diffusion in the vicinity of the kink, exacerbating the differences in lithiation between the

Please cite this article in press as: Andrews et al., Curvature-Induced Modification of Mechano-Electrochemical Coupling and Nucleation Kinetics in a Cathode Material, Matter (2020), https://doi.org/10.1016/j.matt.2020.08.030

concave and convex regions. Local curvature can thus serve to preferentially nucleate Li-ion intercalation, generating hot spots for Li-ion concentrations and driving phase-separation patterns. Notably, SVD analysis (Figure 3) indicates that curvature can induce substantially increased lithiation in V_2O_5; however, in the case of local curvature, hot-spot formation gives rise to local inhomogeneities, since the extent of lithiation in the vicinity of the defect is markedly different from that in the rest of the particle. As such, this observation delineates the need for continuous curvature to homogeneously accelerate lithiation kinetics without accumulating coherency strain across the electrode.

Incorporating Continuous Curvature in Colloidal Crystal Templated Architectures to Improve Phase Homogeneity and Reduce Intercalation-Induced Stress

To incorporate continuous curvature such as to obtain rapid kinetics of Li-ion intercalation without forming local hot spots that result in coherency strain, we have examined the lithiation of continuously curved 3D architectures formed by colloidal crystal templating. Thin-film electrodes constituted from continuously curved V_2O_5 3D architectures show an order-of-magnitude improvement in the Li-ion diffusion constants relative to continuous V_2O_5 thin films in half-cell measurements (D_{Li^+} = 4.7×10^{-13} and 4.6×10^{-10} $cm^2\ s^{-1}$ for continuous film and inverse 3D architectures, respectively),[36,56,57] but the specific physical origins of the improved rate performance and the patterns of phase separation remain to be elucidated. To investigate the role of continuous curvature, we grew V_2O_5 3D architectures (monolayer inverse opal structures) onto silicon nitride substrates as described in Experimental Procedures. Using a modified Langmuir-Blodgett trough method, a monolayer of the inverse opal structure was grown on a substrate that incorporated 2-μm patterned holes in the silicon nitride substrate (same order of magnitude in size as the 2.5-μm polystyrene spheres). Phase-pure α-V_2O_5 structure was confirmed using Raman spectroscopy (Figure S16A). Raman modes were labeled using assignments from previously reported work.[46,58] The morphology and texture of the films was evaluated by SEM (Figure S16B) and TEM (Figure S17). Figure S17 illustrates the formation of single-crystalline domains of V_2O_5 following annealing with the basal planes aligned parallel to the silicon nitride substrate.

As shown in Figure 1, despite lithiation conditions identical to those for the straight and locally curved nanoribbons, the continuously curved patterned architecture exhibits a significantly higher average extent of lithiation, indicative of increased diffusion of Li within the structure. The observed improvement in the kinetics of diffusion derives in part from the porous structure that promotes enhanced electrolyte wetting of the V_2O_5 surface.[36,46,57] In remarkable contrast to the unstrained nanoribbon (Figure 2) and the curved/strained nanoribbon (Figure 3), PCA-clustering analysis of the colloidal crystal templated sample, shown in Figure S18, indicates almost no inhomogeneity locally within ligaments or globally across the imaged area from one honeycomb region to another. Figures S21 and S22 show similar homogeneity for two additional continuously curved 3D architectures prepared by colloidal crystal templating. These additional 3D architectures were lithiated using increased *n*-butyllithium concentrations for extended times (1 h), as described in detail in Supplemental Experimental Procedures, and thereby exhibit a subtly higher degree of lithiation. In contrast to the straight and bent nanoribbons, where distinctive modulations of the relative intensities and peak positions of the V 3d-derived fine structure and O K-edge spectra are observed, these components exhibit few changes in the relevant regions of the V L-/O K-edge spectra. Indeed, the observed spatial correlations delineated in Figure 4 appear to closely approximate the

Please cite this article in press as: Andrews et al., Curvature-Induced Modification of Mechano-Electrochemical Coupling and Nucleation Kinetics in a Cathode Material, Matter (2020), https://doi.org/10.1016/j.matt.2020.08.030

thickness/wall contours of the nanobowl architecture, directly mirroring the thickness maps in Figure 1D and the further detail in Figure S3C. PCA-clustered spectra used as input for SVD mapping are shown in Figure 4A. The V L_3-edge is observed to be relatively featureless and does not exhibit any distinctive fine structure, indicative of a high degree of lithiation, corresponding to the stabilization of highly lithiated ε-$Li_xV_2O_5$ ($x \sim 0.6$) phase.[4,44] Comparison of the spectral features indicates that the spectra differ almost solely in intensity, reflecting differences in film thickness, closely following the contours of the nanobowl architectures as shown in the thickness map in Figure S3C. The cluster intensity maps shown in Figures 4D–4G are arranged in order of increasing thickness (left to right, top to bottom).

We have furthermore performed ROI analysis along various nanobowl contours and across different nanobowl contours, as shown in Figures S19 and S20. The observed ROI-derived spectra are not only consistent within each nanobowl vacancy but also across different nanobowl vacancies. Given the identical lithiation conditions under which the three V_2O_5 morphologies were subjected, the complete absence of inhomogeneity on such a short lithiation time scale not only shows increased rates of lithiation[36,37,56] but also suggests that continuous curvature provides a means to leverage strain-induced improvements in diffusion kinetics while avoiding the hotspot formation induced by local curvature. Compositional homogeneity across nanobowl structures has been observed for additional nanobowl structures lithiated under different conditions, as shown in Figures S21 and S22, which further exhibit spectral differences derived from thickness only.

Quantitative Compositional Mapping and Stress Analysis

Figure S6 illustrates the process by which STXM data (Figure 1) are converted into accurate composition maps depicting the distribution of lithiated V_2O_5 domains and subsequently to von Mises stress maps, as shown in Figures 5 and 6, respectively.[14,20,54] The composition maps exhibit similar trends to the SVD maps shown in Figures 2, 3, and 4 but further take into account spectral weighting across each pixel and thereby provide a quantitative account of the extent of lithiation. Figure 5A shows the core-shell lithiation of the underlying straight nanoribbon (ribbon 1) and a higher extent of lithiation for the top nanoribbon (ribbon 2). The composition map for the bent nanoribbon is shown in Figure 5B and illustrates a relatively greater range of inhomogeneity (x from 0.088 to 0.557 in $Li_xV_2O_5$) as compared with the straight nanoribbons (x from 0.0333 to 0.195 in $Li_xV_2O_5$). Consistent with the analysis in preceding sections, the "hot spot" labeled in the composition map in Figure 5B is located at the crease of the curved defect in the V_2O_5 nanoribbon. This hot spot is surrounded by areas of lower lithiation. Indeed, a "cold spot" is observed on the opposite end, which is under tensile strain. The stark compositional inhomogeneity suggests that the compressive strain resulting at the concave side of the curvature drives more rapid lithiation within about 150 nm of the kink along the surface of the nanoribbon and extending about 60 nm into the nanoribbon. Unlike for the locally curved nanoribbon, no lithiation hot spots are observed to form for the continuously curved architectures prepared by colloidal crystal templating in Figure 5C, which depict a much more homogeneous composition profile corresponding to a single lithiated phase (ε-$Li_xV_2O_5$, Figure 1A). The observed distribution of $Li_xV_2O_5$ phases present in the straight nanoribbon, bent nanoribbon, and the continuously curved architecture are summarized schematically in Figure 5D.

Figures 6A and 6B show von Mises stress maps obtained for the straight and locally curved nanoribbons, respectively, through treatment of the STXM data as described in Experimental Procedures and in Figure S6. The most significant stress

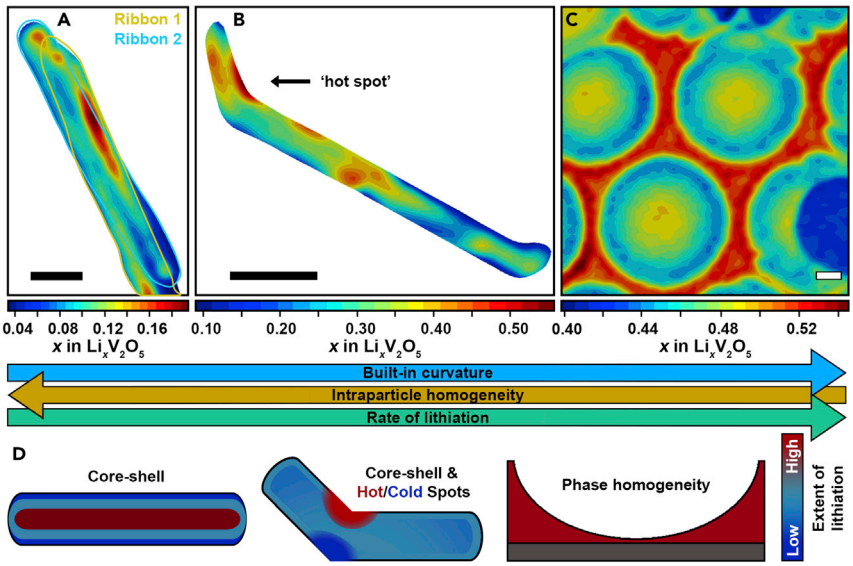

Figure 5. Visualizing Composition in Lithiated V_2O_5 Cathode Materials

(A–C) Composition maps generated from the SVD maps shown in Figures 2D–2F, 3B–3E, and 4D–4G for (A) the straight nanoribbons (B) the locally curved nanoribbon, and (C) the continuously curved V_2O_5 3D architecture. The colored bars below the images correspond to composition of the nanoribbons (i.e., x in $Li_xV_2O_5$). Composition maps were generated by mapping the local stoichiometric fractions determined by assignment of PCA-clustered spectra to a Gauss filter-smoothed image as described in detail in Experimental Procedures and schematically in Figure S6. Scale bars, 500 nm.

(D) Schematic representation summarizing the trends observed across the different geometries.

experienced by the locally curved nanoribbon (Figure 6B) following lithiation coincides with the boundary of the hot spot with the rest of the nanoribbon, reflecting the elastic misfit strain at the interface between high- and low-lithiated domains. In contrast, Figure 6A depicts roughly the core-shell contours of stresses in straight nanoribbons.

The compressive strain induced by the defect in the nanoribbon leads to an increased local rate of lithiation. Additionally the defect, where curvature is highest, promotes surface-limited lithiation, likely serving as a nucleation site for initiation of the phase transformation.[59] The application of strain leads to improved Li-ion diffusion;[15] however, in the case of single defects where curvature-induced strain is highly localized in and around the "defect" (Figures 3 and 6B), this engenders the formation of lithiation hot spots that further have the effect of inducing elastic misfit strain at the interface between the hot spot and adjacent domains with lower extents of lithiation. These observations thus suggest an important role for particle geometry in mitigating the effects of accumulated stresses. The results further suggest the importance of mesoscale structuring to incorporate curvature and strain more globally across the electrode to accelerate diffusion kinetics. Indeed, a simulated stress map for the continuously curved architecture prepared by colloidal crystal templating is shown in Figure 6C. Whereas stress mapping of straight and curved nanoribbons from STXM-derived composition profiles are enabled by their low and uniform thickness normal to the image plane, for continuously curved architectures such as the 3D nanobowl architectures, STXM yields two-dimensional (2D) projections of the compositions. Nevertheless, the composition profiles in Figure 5C along with height maps derived from optical density

Please cite this article in press as: Andrews et al., Curvature-Induced Modification of Mechano-Electrochemical Coupling and Nucleation Kinetics in a Cathode Material, Matter (2020), https://doi.org/10.1016/j.matt.2020.08.030

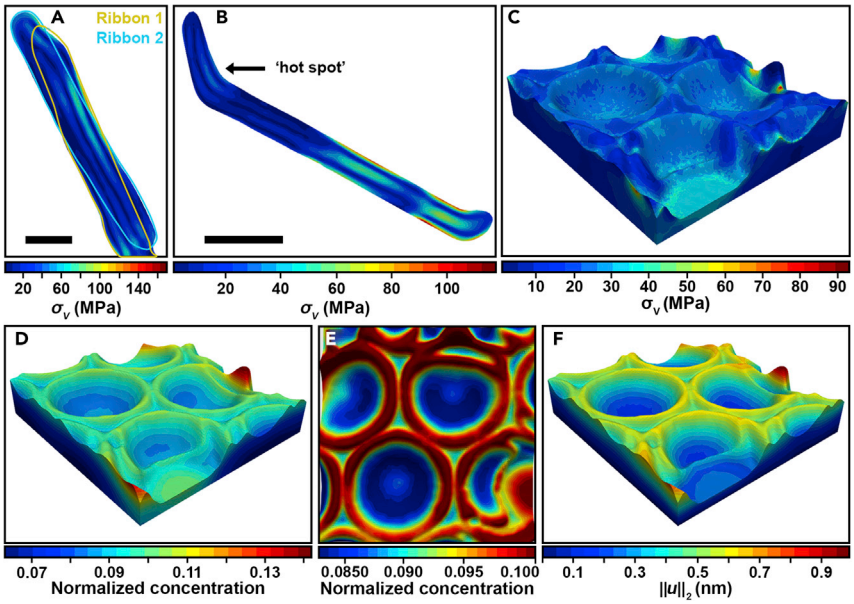

Figure 6. Visualizing Stress Evolution across V_2O_5 Geometries

(A and B) Von Mises stress maps generated from the composition maps shown in Figure 5 for (A) the straight nanoribbons and (B) the locally curved nanoribbon. Scale bars, 500 nm.

(C) Stress map derived from a finite element simulation from an optical density-derived thickness map.

(D) Normalized equilibrium concentration resulting from the finite element simulation, which shows that under an applied chemical potential (shown here for t = 449 s), Li redistributes across the continuously curved V_2O_5 3D architecture.

(E) A 2D top-down view of the 3D mesh shown in (D) capturing the phase composition map observed from STXM in Figure 5C. Mesh generation from the thickness data is described in Figure S23.

(F) The displacement of the mesh normal to the substrate during lithiation, which enables relaxation of stresses by dint of the geometric curvature.

(Figure S3) enable the construction of 3D finite element meshes. Stress maps derived from such meshes as described in Supplemental Experimental Procedures (see also Figure S23) for the 3D continuously curved architectures show substantially reduced stresses as compared with the straight and locally curved geometries, concordant with the substantially greater compositional and phase homogeneity observed in the STXM maps (Figures 6D and 6E show the 3D simulated composition mesh, which accurately captures the experimental concentration distribution in Figure 5C). Figure 6F illustrates that the unconstrained expansion of the continuously curved architectures allows for facile relaxation of intercalation-induced stresses in this geometry. The deformation is observed to be largest at the centers of the nanobowl ridges since, when ascending from the nanobowl centers to the ridge maxima, the structure becomes progressively thinner and thus exerts less resistance to deformation. This further allows for a relaxation of the diffusion-induced stresses within the structure. The ability of the patterned electrode to relax stresses is a strong advantage over planar thin-film electrodes (and even porous high-capacity electrodes), where strong directional stresses have been known to cause strong mechanical degradation.[60,61] Incorporating continuous curvature, as in the case of the continuously curved 3D V_2O_5 architecture, thereby yields a much higher extent of lithiation (Figure 1) while retaining homogeneity across extended domains, thereby mitigating the evolution of lattice coherency strain.

Please cite this article in press as: Andrews et al., Curvature-Induced Modification of Mechano-Electrochemical Coupling and Nucleation Kinetics in a Cathode Material, Matter (2020), https://doi.org/10.1016/j.matt.2020.08.030

Conclusions

Inhomogeneous volume expansion in the electrode materials of Li-ion batteries is often implicated in the degradation of cell performance. In cathode materials where Li-ion intercalation induces phase transformations, lithiation inhomogeneities within individual particles can give rise to substantial lattice coherency strain. The value of the von Mises stress at a given point reflects the relative compression of the crystal lattice as a result of the lithiation fraction within the matrix and is correlated with and interdependent on the local environment, not just the concentration alone. Elastic misfit stresses and strains at the boundaries of phase-segregated domains can suppress Li-ion diffusion, and the accumulated stresses bring about plastic deformation and fracture of cathode particles. As a corollary, the application of modest directional lattice strain in thin-film cathodes can modify atomistic structure and reduce migration barriers for Li-ion diffusion,[15] enabling improved rate performance. However, these approaches rely on the application of strain through epitaxial interfaces.

Here, we illustrate the quantitative mapping of Li-ion compositions and stress magnitudes within individual particles, ensembles of particles, and across architected electrodes of V_2O_5 using STXM to map the distinctive spectroscopic signatures of variously lithiated $Li_xV_2O_5$ phases. In V_2O_5 nanoribbons, surface-limited lithiation follows a core-shell pattern. However, in the presence of kinks derived from stacking faults, local curvature serves to preferentially nucleate lithiation along the concave inner surface while diminishing lithiation along the convex outer surface. The vastly amplified inhomogeneity of lithiation results is mapped as large von Mises stresses along the interface between low- and high-lithiated domains. The introduction of continuous curvature within colloidal crystal templated nanobowl architectures allows for homogeneous and substantially enhanced kinetics of lithiation, mitigating the stress gradients that inevitably arise from local inhomogeneities and elastic misfit strains. Notably, this study has focused on examining the evolution of stress across different geometries during lithiation at the equivalent of low C-rates, whereby kinetic phenomena and surface-reaction-limited processes dominate over diffusion-limited processes.[14,20,52,62,63] For phase-separating materials, such a phenomenon yields morphologies with distinctive intercalation/reaction fronts that reflect nucleation of the lithiated phase at specific sites within the particle (e.g., asperities, defects, and edges have a high potency of nucleation). At high current densities or after nucleation restrictions have been overcome, a diffusion-limited regime is observed.[52] As such, during lithiation the resistance of the electrolyte interface, rather than the concentration resistance within the active particle, governs the morphology and shape of the reaction front.[49] In contrast, during delithiation, in the absence of nucleation limitations and given the higher degree of compositional inhomogeneity than at the onset of lithiation, thermodynamic considerations are expected to be dominant, allowing for observation of spinodal decomposition patterns.[62–64] Indeed, recent lithiation/delithiation studies of single crystals of ζ-V_2O_5 even suggest that Li ions prefer a specific ordering of crystallographic sites upon lithiation (β/β′/C site fill in a specific order), but Li is removed from all sites at the same time during delithiation.[65] It is expected that the evolution of stress derived from compositional inhomogeneity would be exacerbated during delithiation owing to increased rates of delithiation from hot spots formed during lithiation.[62] Mitigating stress during delithiation (charging) provides further motivation for incorporating geometric curvature into the mesoscale design of cathode materials. The results presented here demonstrate the potential for using mesostructured architectures such as continuously curved nanobowls to incorporate continuous curvature and provide a promising route to leveraging electrochemistry-mechanics coupling to improve the electrochemical performance of cathode

Please cite this article in press as: Andrews et al., Curvature-Induced Modification of Mechano-Electrochemical Coupling and Nucleation Kinetics in a Cathode Material, Matter (2020), https://doi.org/10.1016/j.matt.2020.08.030

materials. The mitigation of failure mechanisms derived from elastic misfit strain is typically achieved by sacrificing the kinetics of lithiation (e.g., charge rate). Here we demonstrate how continuous curvature can be leveraged to simultaneously enable fast Li-ion diffusion kinetics and alleviate mechanical stresses developed during lithiation.

EXPERIMENTAL PROCEDURES

Resource Availability

Lead Contact

Sarbajit Banerjee (email: banerjee@chem.tamu.edu).

Materials Availability

This study did not generate new unique materials.

Data and Code Availability

All experimental data, computational data, and code are available upon reasonable request to the Lead Contact author.

Synthesis of V_2O_5 Nanoribbons and Continuously Curved V_2O_5 3D Architectures

V_2O_5 nanoribbons were synthesized by adaptation of a previously reported method comprising hydrothermal growth of $V_3O_7{\cdot}H_2O$ nanoribbons followed by low-temperature calcination in air to V_2O_5.[46] Further details related to the synthesis of V_2O_5 nanoribbons and their characterization (e.g., XRD, TEM, SEM) are detailed in Supplemental Experimental Procedures.

V_2O_5 nanobowl 3D architectures were prepared by the adaptation of a previously reported method.[36] In brief, polystyrene microspheres were deposited onto a silicon nitride grid using a modified Blodgett trough method. The interstices of the closely packed structure were infiltrated with a vanadium oxide sol, which was allowed to gel by controlled exposure to ambient humidity. The gel was annealed and calcined to remove the polystyrene microspheres. The growth of the colloidal crystal templated films was limited to a single monolayer of polystyrene microspheres. and thus the growth of a true inverse opal structure was prevented. As such, the 3D architecture is here termed as a "nanobowl" architecture. Further details pertaining to the synthesis and characterization of V_2O_5 inverse opal structures (e.g., Raman, TEM, SEM) are provided in Supplemental Experimental Procedures.

"On-Substrate" Chemical Lithiation of V_2O_5 Nanoribbons and 3D Architectures

A well-established chemical lithiation approach[20,46,66] was adapted in this work to facilitate the identification of nanoribbons with distinctive defects and their analysis by STXM. This process is illustrated schematically in Figure S5 and described in greater detail in Supplemental Experimental Procedures.

Scanning Transmission X-Ray Microscopy and Compositional and Strain Maps Workflow

STXM data were collected at the spectromicroscopy beamline 10ID-1 of the Canadian Light Source (Saskatoon, SK, Canada). STXM data were analyzed using the aXis2000 software suite (version updated October 11, 2019; download: http://unicorn.mcmaster.ca/aXis2000.html). The workflow of STXM data collection and processing to obtain compositional and strain maps employed in this work are

shown schematically in Figure S6 and described in greater detail in Supplemental Experimental Procedures.

Chemomechanical Finite Element Simulation

To investigate the evolution of stress in the markedly 3D nanobowl architecture, we performed 3D electrochemical simulations on a finite element mesh constructed using STXM thickness maps according to a previously described method.[57] Further details of the method employed for these simulations is described in greater detail in Supplemental Experimental Procedures and Figure S23.

SUPPLEMENTAL INFORMATION

Supplemental Information can be found online at https://doi.org/10.1016/j.matt.2020.08.030.

ACKNOWLEDGMENTS

This study is based on work supported by the National Science Foundation (NSF) under DMR 1809866. J.L.A. acknowledges support from a NASA Space Technology Research Fellowship under grant no. 80NSSC17K0182. D.A.S. acknowledges support under an NSF Graduate Research Fellowship under grant no. 1746932. P.S. and B.-X.X. acknowledge the German Science Foundation for financial support on the project STE2350/1-1 with the number 398072825. M.P. acknowledges support from the NSF under DMR 1944674. A large portion of the research described in this article was performed at the Canadian Light Source (SM beamline, 10ID-1), which is supported by the Natural Sciences and Engineering Research Council of Canada, the National Research Council Canada, the Canadian Institutes of Health Research, the Province of Saskatchewan, Western Economic Diversification Canada, and the University of Saskatchewan. Use of the TAMU Materials Characterization Facility is acknowledged. Use of the Texas A&M Microscopy and Imaging Center is acknowledged.

AUTHOR CONTRIBUTIONS

Conceptualization, J.L.A., M.P., J.D.B., B.-X.X., and S.B.; Methodology, J.L.A., P.S., and D.A.S.; Software, P.S. and B.-X.X.; Formal Analysis, J.L.A., P.S., and D.A.S.; Investigation, J.L.A., P.S., D.A.S., C.J.C., L.R.D.J., R.D.D., and M.A.G.; Resources, J.D.B., B.-X.X., and S.B.; Writing – Original Draft, J.L.A., P.S., D.A.S., B.-X.X., and S.B.; Writing – Review & Editing, J.L.A., C.J.C., R.D.D., M.P., J.D.B., B.-X.X., and S.B.; Visualization, J.L.A. and P.S.; Supervision, M.P., J.D.B., B.-X.X., and S.B.; Project Administration, S.B.; Funding Acquisition, B.X.-X. and S.B.

DECLARATION OF INTERESTS

The authors declare no competing interests.

Received: June 3, 2020
Revised: August 9, 2020
Accepted: August 27, 2020
Published: September 23, 2020

REFERENCES

1. Whittingham, M.S. (2004). Lithium batteries and cathode materials. Chem. Rev. *104*, 4271–4301.

2. Goodenough, J.B., and Park, K.-S. (2013). The Li-ion rechargeable battery: a perspective. J. Am. Chem. Soc. *135*, 1167–1176.

3. Marianetti, C.A., Kotliar, G., and Ceder, G. (2004). A first-order Mott transition in Li_xCoO_2. Nat. Mater. *3*, 627–631.

4. De Jesus, L.R., Andrews, J.L., Parija, A., and Banerjee, S. (2018). Defining diffusion pathways in intercalation cathode materials: some lessons from V_2O_5 on directing cation traffic. ACS Energy Lett. *3*, 915–931.

5. Stein, P., Zhao, Y., and Xu, B.X. (2016). Effects of surface tension and electrochemical reactions

in Li-ion battery electrode nanoparticles. J. Power Sources *332*, 154–169.

6. Zhao, Y., Stein, P., Bai, Y., Al-Siraj, M., Yang, Y., and Xu, B.X. (2019). A review on modeling of electro-chemo-mechanics in lithium-ion batteries. J. Power Sources *413*, 259–283.

7. Chan, C.K., Peng, H., Liu, G., Mcilwrath, K., Zhang, X.F., Huggins, R.A., and Cui, Y. (2008). High-performance lithium battery anodes using silicon nanowires. Nat. Nanotechnol. *3*, 31–35.

8. Hardin, G.R., Zhang, Y., Fincher, C.D., and Pharr, M. (2017). Interfacial fracture of nanowire electrodes of lithium-ion batteries. JOM *69*, 1519–1523.

9. Mukhopadhyay, A., and Sheldon, B.W. (2014). Deformation and stress in electrode materials for Li-ion batteries. Prog. Mater. Sci. *63*, 58–116.

10. Lewis, J.A., Tippens, J., Cortes, F.J.Q., and McDowell, M.T. (2019). Chemo-mechanical challenges in solid-state batteries. Trends Chem. *1*, 845–857.

11. Thackeray, M.M. (1995). Structural considerations of layered and spinel lithiated oxides for lithium ion batteries. J. Electrochem. Soc. *142*, 2558–2563.

12. Reimers, J.N., and Dahn, J.R. (1992). Electrochemical and in situ X-Ray diffraction studies of lithium intercalation in Li_xCoO_2. J. Electrochem. Soc. *139*, 2091–2097.

13. Padhi, A.K., Nanjundaswamy, K.S., and Goodenough, J.B. (1997). Phospho-olivines as positive-electrode materials for rechargeable lithium batteries. J. Electrochem. Soc. *144*, 1188–1194.

14. De Jesus, L.R., Stein, P., Andrews, J.L., Luo, Y., Xu, B., and Banerjee, S. (2018). Striping modulations and strain gradients within individual particles of a cathode material upon lithiation. Mater. Horiz. *5*, 486–498.

15. Muralidharan, N., Brock, C.N., Cohn, A.P., Schauben, D., Carter, R.E., Oakes, L., Walker, D.G., and Pint, C.L. (2017). Tunable mechanochemistry of lithium battery electrodes. ACS Nano *11*, 6243–6251.

16. Ning, F., Li, S., Xu, B., and Ouyang, C. (2014). Strain tuned Li diffusion in $LiCoO_2$ material for Li ion batteries: a first principles study. Solid State Ionics *263*, 46–48.

17. Tealdi, C., Heath, J., and Islam, M.S. (2016). Feeling the strain: enhancing ionic transport in olivine phosphate cathodes for Li- and Na-ion batteries through strain effects. J. Mater. Chem. A *4*, 6998–7004.

18. Zhang, Y., Luo, Y., Fincher, C., Banerjee, S., and Pharr, M. (2019). Chemo-mechanical degradation in V_2O_5 thin film cathodes of Li-ion batteries during electrochemical cycling. J. Mater. Chem. A *7*, 23922–23930.

19. Bucci, G., Swamy, T., Bishop, S., Sheldon, B.W., Chiang, Y.-M., and Carter, W.C. (2017). The effect of stress on battery-electrode capacity. J. Electrochem. Soc. *164*, A645–A654.

20. De Jesus, L.R., Zhao, Y., Horrocks, G.A., Andrews, J.L., Stein, P., Xu, B.-X.B., and Banerjee, S. (2017). Lithiation across interconnected V_2O_5 nanoparticle networks. J. Mater. Chem. A *5*, 20141–20152.

21. Zhao, Y., De Jesus, L.R., Stein, P., Horrocks, G.A., Banerjee, S., and Xu, B.-X. (2017). Modeling of phase separation across interconnected electrode particles in lithium-ion batteries. RSC Adv. *7*, 41254–41264.

22. Li, D., and Zhou, H. (2014). Two-phase transition of Li-intercalation compounds in Li-ion batteries. Mater. Today *17*, 451–463.

23. Boesenberg, U., Meirer, F., Liu, Y., Shukla, A.K., Dell'Anna, R., Tyliszczak, T., Chen, G., Andrews, J.C., Richardson, T.J., Kostecki, R., and Cabana, J. (2013). Mesoscale phase distribution in single particles of $LiFePO_4$ following lithium deintercalation. Chem. Mater. *25*, 1664–1672.

24. Zhu, Y., and Wang, C. (2011). Strain accommodation and potential hysteresis of $LiFePO_4$ cathodes during lithium ion insertion/extraction. J. Power Sources *196*, 1442–1448.

25. Ulvestad, A., Singer, A., Cho, H.M., Clark, J.N., Harder, R., Maser, J., Meng, Y.S., and Shpyrko, O.G. (2014). Single particle nanomechanics in operando batteries via lensless strain mapping. Nano Lett. *14*, 5123–5127.

26. Cogswell, D.A., and Bazant, M.Z. (2012). Coherency strain and the kinetics of phase separation in $LiFePO_4$ nanoparticles. ACS Nano *6*, 2215–2225.

27. Tippens, J., Miers, J.C., Afshar, A., Lewis, J.A., Cortes, F.J.Q., Qiao, H., Marchese, T.S., Di Leo, C.V., Saldana, C., and McDowell, M.T. (2019). Visualizing chemomechanical degradation of a solid-state battery electrolyte. ACS Energy Lett. *4*, 1475–1483.

28. Zhao, K., Pharr, M., Hartle, L., Vlassak, J.J., and Suo, Z. (2012). Fracture and debonding in lithium-ion batteries with electrodes of hollow core-shell nanostructures. J. Power Sources *218*, 6–14.

29. Song, H., Jeong, T.G., Yun, S.W., Lee, E.K., Park, S.A., and Kim, Y.T. (2017). An upper limit of Cr-doping level to retain zero-strain characteristics of $Li_4Ti_5O_{12}$ anode material for Li-ion batteries. Sci. Rep. *7*, 43335.

30. Kim, U.H., Myung, S.T., Yoon, C.S., and Sun, Y.K. (2017). Extending the battery life using an Al-doped $Li[Ni_{0.7}Co_{0.09}Mn_{0.15}]O_2$ cathode with concentration gradients for lithium ion batteries. ACS Energy Lett. *2*, 1848–1854.

31. Andrews, J.L., Mukherjee, A., Yoo, H.D., Parija, A., Marley, P.M., Fakra, S., Prendergast, D., Cabana, J., Klie, R.F., and Banerjee, S. (2018). Reversible Mg-ion insertion in a metastable one-dimensional polymorph of V_2O_5. Chem *4*, 564–585.

32. Parija, A., Liang, Y., Andrews, J.L., De Jesus, L.R., Prendergast, D., and Banerjee, S. (2016). Topochemically de-intercalated phases of V_2O_5 as cathode materials for multivalent intercalation batteries: a first-principles evaluation. Chem. Mater. *28*, 5611–5620.

33. Tepavcevic, S., Liu, Y., Zhou, D., Lai, B., Maser, J., Zuo, X., Chan, H., Král, P., Johnson, C.S., Stamenkovic, V., et al. (2015). Nanostructured layered cathode for rechargeable Mg-ion batteries. ACS Nano *9*, 8194–8205.

34. Tolhurst, T.M., Leedahl, B., Andrews, J.L., Marley, P.M., Banerjee, S., and Moewes, A. (2016). Contrasting 1D tunnel-structured and 2D layered polymorphs of V_2O_5: relating crystal structure and bonding to band gaps and electronic structure. Phys. Chem. Chem. Phys. *18*, 15798–15806.

35. Su, L., Jing, Y., and Zhou, Z. (2011). Li ion battery materials with core-shell nanostructures. Nanoscale *3*, 3967–3983.

36. Chalker, C.J., An, H., Zavala, J., Parija, A., Banerjee, S., Lutkenhaus, J.L., and Batteas, J.D. (2017). Fabrication and electrochemical performance of structured mesoscale open shell V_2O_5 networks. Langmuir *33*, 5975–5981.

37. Li, L., Steiner, U., and Mahajan, S. (2010). Improved electrochromic performance in inverse opal vanadium oxide films. J. Mater. Chem. *20*, 7131–7134.

38. De Jesus, L.R., Horrocks, G.A., Liang, Y., Parija, A., Jaye, C., Wangoh, L., Wang, J., Fischer, D.A., Piper, L.F.J., Prendergast, D., and Banerjee, S. (2016). Mapping polaronic states and lithiation gradients in individual V_2O_5 nanowires. Nat. Commun. *7*, 12022.

39. Ellis, B., Perry, L.K., Ryan, D.H., and Nazar, L.F. (2006). Small polaron hopping in $Li_x FePO_4$ solid solutions: coupled lithium-ion and electron mobility. J. Am. Chem. Soc. *128*, 11416–11422.

40. Watthaisong, P., Jungthawan, S., Hirunsit, P., and Suthirakun, S. (2019). Transport properties of electron small polarons in a V_2O_5 cathode of Li-ion batteries: a computational study. RSC Adv. *9*, 19483–19494.

41. Lee, J., Pennycook, S.J., and Pantelides, S.T. (2012). Simultaneous enhancement of electronic and Li^+ ion conductivity in $LiFePO_4$. Appl. Phys. Lett. *101*, https://doi.org/10.1063/1.4737212.

42. Muralidharan, N., Carter, R., Oakes, L., Cohn, A.P., and Pint, C.L. (2016). Strain engineering to modify the electrochemistry of energy storage electrodes. Sci. Rep. *6*, 27542.

43. Satto, C., Sciau, P., Dooryhee, E., Galy, J., and Millet, P. (1999). The $\delta \rightarrow \varepsilon \rightarrow \gamma$ LiV_2O_5 "'high temperature"' phase transitions evidenced by synchrotron X-ray powder diffraction analysis. J. Solid State Chem. *109*, 103–109.

44. Horrocks, G.A., De Jesus, L.R., Andrews, J.L., and Banerjee, S. (2017). X-ray spectroscopy and imaging as multiscale probes of intercalation phenomena in cathode materials. JOM *69*, 1469–1477.

45. Luo, Y., De Jesus, L.R., Andrews, J.L., Parija, A., Fleer, N., Robles, D.J., Mukherjee, P.P., and Banerjee, S. (2018). Roadblocks in cation diffusion pathways: implications of phase boundaries for Li-ion diffusivity in an intercalation cathode material. ACS Appl. Mater. Inter. *10*, 30901–30911.

46. Horrocks, G.A., Likely, M.F., Velazquez, J.M., and Banerjee, S. (2013). Finite size effects on the structural progression induced by lithiation of V_2O_5: a combined diffraction and Raman spectroscopy study. J. Mater. Chem. A *1*, 15265–15277.

47. Maganas, D., Roemelt, M., Hävecker, M., Trunschke, A., Knop-Gericke, A., Schlögl, R.,

and Neese, F. (2013). First principles calculations of the structure and V L-edge X-ray absorption spectra of V_2O_5 using local pair natural orbital coupled cluster theory and spin-orbit coupled configuration interaction approaches. Phys. Chem. Chem. Phys. *15*, 7260–7276.

48. Lerotic, M., Jacobsen, C., Gillow, J.B., Francis, A.J., Wirick, S., Vogt, S., and Maser, J. (2005). Cluster analysis in soft X-ray spectromicroscopy: finding the patterns in complex specimens. J. Electron Spectros. Relat. Phenom. *144–147*, 1137–1143.

49. Mistry, A.N., Smith, K., and Mukherjee, P.P. (2018). Secondary-phase stochastics in lithium-ion battery electrodes. ACS Appl. Mater. Interfaces *10*, 6317–6326.

50. Li, Y., El Gabaly, F., Ferguson, T.R., Smith, R.B., Bartelt, N.C., Sugar, J.D., Fenton, K.R., Cogswell, D.A., Kilcoyne, A.L.D., Tyliszczak, T., et al. (2014). Current-induced transition from particle-by-particle to concurrent intercalation in phase-separating battery electrodes. Nat. Mater. *13*, 1149–1156.

51. Mistry, A., Usseglio-Viretta, F.L.E., Colclasure, A., Smith, K., and Mukherjee, P.P. (2020). Fingerprinting redox heterogeneity in electrodes during extreme fast charging. J. Electrochem. Soc. *167*, 090542.

52. Fraggedakis, D., Nadkarni, N., Gao, T., Zhou, T., Zhang, Y., Han, Y., Stephens, R.M., Shao-Horn, Y., and Bazant, M.Z. (2020). A scaling law to determine phase morphologies during ion intercalation. Energy Environ. Sci. https://doi.org/10.1039/d0ee00653j.

53. Mistry, A., Smith, K., and Mukherjee, P.P. (2020). Stochasticity at scales leads to lithium intercalation cascade. ACS Appl. Mater. Interfaces *12*, 16359–16366.

54. Zhao, Y., Xu, B.X., Stein, P., and Gross, D. (2016). Phase-field study of electrochemical reactions at exterior and interior interfaces in Li-ion battery electrode particles. Comput. Methods Appl. Mech. Eng. *312*, 428–446.

55. Boebinger, M.G., Yeh, D., Xu, M., Miles, B.C., Wang, B., Papakyriakou, M., Lewis, J.A., Kondekar, N.P., Cortes, F.J.Q., Hwang, S., et al. (2018). Avoiding fracture in a conversion battery material through reaction with larger ions. Joule *2*, 1783–1799.

56. Armstrong, E., McNulty, D., Geaney, H., and ODwyer, C. (2015). Electrodeposited structurally stable V_2O_5 inverse opal networks as high performance thin film lithium batteries. ACS Appl. Mater. Interfaces *7*, 27006–27015.

57. Stein, P., Wissel, S., and Xu, B.-X. (2020). The influence of surface stress on the chemo-mechanical behavior of inverse-opal structured electrodes for lithium-ion batteries. J. Electrochem. Soc. *167*, 013529.

58. Baddour-hadjean, R., and Pereira-Ramos, J.-P. (2008). Raman microspectrometry applied to the study of electrode materials for lithium batteries. Chem. Rev. *110*, 1278–1319.

59. Hudak, B.M., Depner, S.W., Waetzig, G.R., Talapatra, A., Arroyave, R., Banerjee, S., and Guiton, B.S. (2017). Real-time atomistic observation of structural phase transformations in individual hafnia nanorods. Nat. Commun. *8*, 15316.

60. Beaulieu, L.Y., Eberman, K.W., Turner, R.L., Krause, L.J., and Dahna, J.R. (2001). Colossal reversible volume changes in lithium alloys. Electrochem. Solid State Lett. *4*, 7–10.

61. Barai, P., and Mukherjee, P.P. (2016). Mechano-electrochemical stochastics in high-capacity electrodes for energy storage. J. Electrochem. Soc. *163*, A1120–A1137.

62. Lim, J., Li, Y., Alsem, D.H., So, H., Lee, S.C., Bai, P., Cogswell, D.A., Liu, X., Jin, N., Yu, Y.S., et al. (2016). Origin and hysteresis of lithium compositional spatiodynamics within battery primary particles. Science *353*, 566–571.

63. Bazant, M.Z. (2017). Thermodynamic stability of driven open systems and control of phase separation by electro-autocatalysis. Faraday Discuss. *199*, 423–463.

64. Nadkarni, N., Rejovitsky, E., Fraggedakis, D., Di Leo, C.V., Smith, R.B., Bai, P., and Bazant, M.Z. (2018). Interplay of phase boundary anisotropy and electro-auto-catalytic surface reactions on the lithium intercalation dynamics in Li_xFePO_4 plateletlike nanoparticles. Phys. Rev. Mater. *2*, 085406.

65. Handy, J.V., Luo, Y., Andrews, J., Bhuvanesh, N., and Banerjee, S. (2020). An atomic view of cation diffusion pathways from single-crystal topochemical transformations. Angew. Chem. Int. Ed. *59*, https://doi.org/10.1002/anie.202005513.

66. Whittingham, M.S., and Dines, M.B. (1977). *n*-Butyllithium—an effective, general cathode screening agent. J. Electrochem. Soc. *124*, 1387–1388.